

Study of liquid jet instability by confocal microscopy

Cite as: Rev. Sci. Instrum. **83**, 073104 (2012); <https://doi.org/10.1063/1.4734017>

Submitted: 11 April 2012 . Accepted: 22 June 2012 . Published Online: 16 July 2012

Lisong Yang, Leanne J. Adamson and Colin D. Bain



View Online



Export Citation

ARTICLES YOU MAY BE INTERESTED IN

[Determination of dynamic surface tension and viscosity of non-Newtonian fluids from drop oscillations](#)

Physics of Fluids **26**, 113103 (2014); <https://doi.org/10.1063/1.4901823>

[Spatial instability of a jet](#)

The Physics of Fluids **16**, 2052 (1973); <https://doi.org/10.1063/1.1694264>

[Effects of drive amplitude on continuous jet break-up](#)

Physics of Fluids **31**, 064104 (2019); <https://doi.org/10.1063/1.5099016>



PFEIFFER VACUUM

Your Leak Detection Experts

The widest offer of leak testing solutions, using helium and hydrogen



Learn more!



Study of liquid jet instability by confocal microscopy

Lisong Yang, Leanne J. Adamson, and Colin D. Bain

Department of Chemistry, Durham University, South Road, Durham DH1 3LE, United Kingdom

(Received 11 April 2012; accepted 22 June 2012; published online 16 July 2012)

The instability of a liquid microjet was used to measure the dynamic surface tension of liquids at the surface ages of ≤ 1 ms using confocal microscopy. The reflected light from a laser beam at normal incidence to the jet surface is linear in the displacement of the surface near the confocal position, leading to a radial resolution of 4 nm and a dynamic range of 4 μm in the surface position, thus permitting the measurement of amplitude of oscillation at the very early stage of jet instability. For larger oscillations outside the linear region of the confocal response, the swell and neck position of the jet can be located separately and the amplitude of oscillation determined with an accuracy of 0.2 μm . The growth rate of periodically perturbed water and ethanol/water mixture jets with a 100- μm diameter nozzle and mean velocity of 5.7 m s^{-1} has been measured. The dynamic surface tension was determined from the growth rate of the instability with a linear, axisymmetric, constant property model. Synchronisation of the confocal imaging system with the perturbation applied to the jet permitted a detailed study of the temporal evolution of the neck into a ligament and eventually into a satellite drop. © 2012 American Institute of Physics. [<http://dx.doi.org/10.1063/1.4734017>]

I. INTRODUCTION

The formation of drops from streams of liquid has fascinated natural scientists for centuries. The capillary instability that leads to the breakup of a liquid stream has been exploited in many industrial and agricultural processes, including inkjet printing, spraying, and fiber spinning.¹ Lord Rayleigh first pointed out that the instability is caused by surface tension working against inertia. In his linear instability analysis, Rayleigh showed that for a cylindrical jet of an incompressible inviscid liquid, axisymmetric surface oscillations grow exponentially in time when the wavelength λ of the oscillation is greater than the circumference of the undisturbed jet.^{2,3} This oscillation leads to breakup of the jet into drops. Much theoretical and experimental work has since been done on the capillary instability, especially in the vicinity of breakup where the dynamics are nonlinear.¹ It is not yet possible to describe fully the jet dynamics under various fluid conditions and further development of theoretical models and experimental techniques with higher spatial and temporal resolution is ongoing.

The most common experimental setup for studying drop formation in a fast-moving jet is a stroboscopic method where pulsed illumination is synchronised with drop generation.⁴ The typical light duration of 1 μs causes blurring for a jet speed of the order of 10 m s^{-1} and a drop size of a few tens of micrometers. A single-flash imaging technique has been reported in which a 20-ns flash light with high intensity gives a frozen image with much less blur.⁵ Ultrafast laser pulses can also be used in principle to freeze the motion of the jet.^{6,7} The stroboscopic technique requires high drop reproducibility in order to provide a pseudo-sequence of images for the study of the drop formation. Alternatively, high speed cameras can be used to study the evolution of single drops. A camera with a CMOS sensor allows individual access and readout of chips and gives a typical frame rate of a few thousand frames per second for a resolution of 1×10^6 pixels.^{7,8} CCD cameras

with an *in situ* storage image sensor can yield a frame rate of 1×10^6 pixels per second with superior image quality.^{9,10} Recent advances in the speed and resolution of jet imaging have followed on the heels of improvements in sensor and camera technology. A conventional microscope is, however, invariably used to magnify the image of micrometer-sized jets or drops. The spatial lateral resolution R_L depends on the optical system and is diffraction limited to $0.61\lambda_L/\text{NA}$, while λ_L is the wavelength of the illumination and NA is the numerical aperture of the objective lens. For a typical setup using an objective lens with NA of 0.1 and white light illumination, $R_L \approx 3 \mu\text{m}$. In this paper, we demonstrate that confocal imaging permits the study of jet instability with much higher spatial resolution. The temporal resolution of a confocal imaging system is limited by the response time of the photomultiplier tube and by the oscilloscope bandwidth, typically to 1 ns. Confocal imaging is simple and inexpensive to set up and is a valuable complementary tool to conventional imaging.

In confocal microscopy, invented by Minsky in 1957, a pinhole is placed conjugate to the focus of the objective lens so that blurring of the image by out-of-focus signal is efficiently suppressed.¹¹ Confocal microscopy is now widely used as a non-invasive method for generating images of three-dimensional objects.^{12,13} A confocal microscope has a lateral resolution 30% better than a conventional one, i.e., $R_{L\text{-confocal}} = 0.44 \lambda_L/\text{NA}$.¹² Its depth discrimination also provides us with a method to profile surface roughness with nanometer resolution by both interferometric¹⁴ and non-interferometric methods.¹⁵ Here, we use confocal imaging to determine the surface profile of a periodically disturbed jet, from nozzle to breakup. The growth rate of the Rayleigh instability is then used to deduce the dynamic surface tension (DST) of the liquid, following an existing linear, axisymmetric, constant-property model. We validate the measurement technique with ultra-high quality water and ethanol, for which the surface tension may be assumed to be independent of surface age

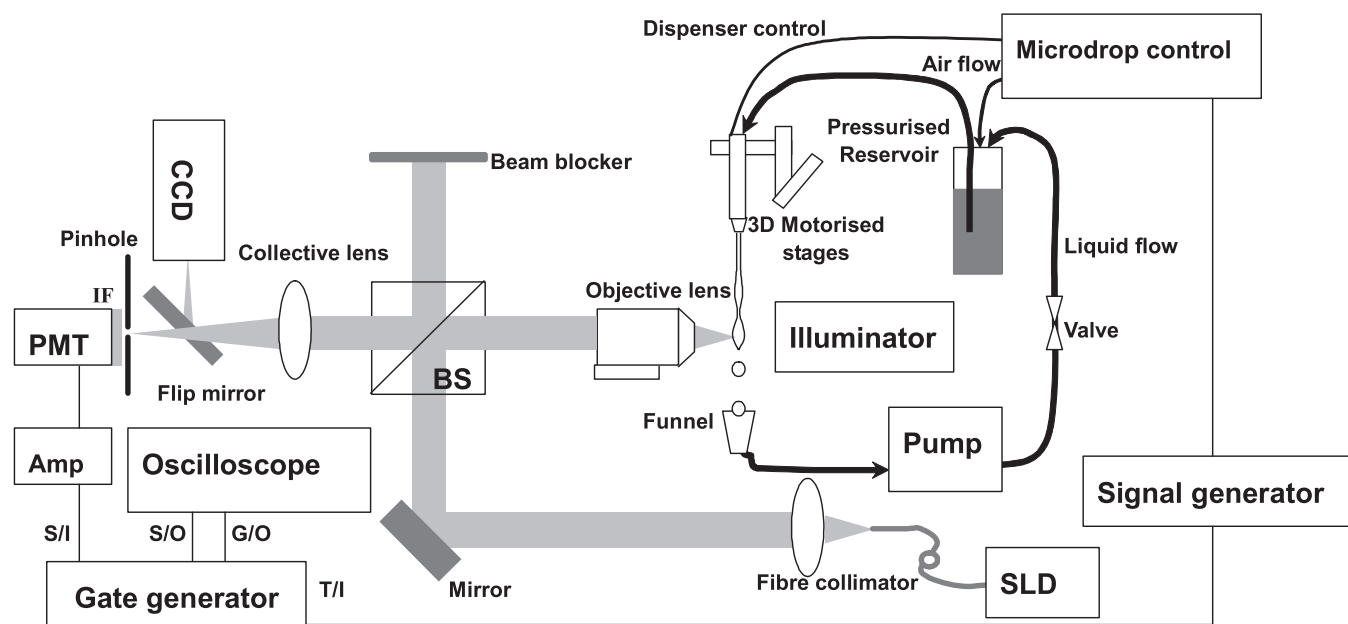


FIG. 1. Schematic of experimental setup for jet instability measurement. SLD: superluminescent diode; BS: beamsplitter; IF: interference filter; PMT: photomultiplier tube; Amp: amplifier. S/I: signal-in; S/O: signal-out; T/I: trigger-in; G/O: gate-out.

on any timescale relevant to isothermal liquid jets, and on ethanol/water mixtures. Preliminary data on surfactant solutions, in which the DST cannot be assumed to be constant, have recently been presented.¹⁶ We also show that confocal microscopy can be used to investigate the temporal evolution of a ligament as it evolves from a neck into a satellite drop.

II. EXPERIMENTAL APPARATUS

Figure 1 shows a schematic of the experimental apparatus for the measurement of jet instabilities. The pressurised liquid is fed from a 200-ml reservoir into a dispenser head (MJ-K-301, Microdrop Technologies GmbH) with a microvalve designed to switch the flow on and off. A pressure control unit (MJ-E-130, Microdrop Technologies GmbH) and a liquid pump are adjusted to keep the reservoir liquid volume constant so as to guarantee a constant liquid flow rate. A laminar jet emerges vertically from the dispenser head with a circular funnel-shaped glass nozzle of 100- μm internal diameter (Fig. 2) into free air with a room temperature of 22 °C. For a reservoir pressure of 0.3 bar, the aqueous jet runs at a mean speed of 5.7 m s⁻¹. The jet is mounted on a 3-axis motorised, translation stage with an actuator travel range of 12.5 mm and an accuracy of 0.2 μm . A transistor-transistor logic (TTL) signal is applied to the valve control inside the dispenser head with a frequency of 10–12 kHz. The valve opens fully when the TTL signal level is high but can only close partially when the TTL signal is low because the applied signal changes faster than the response time of the valve. The control value therefore provides a periodic perturbation on the jet. The mean speed of the jet with the applied perturbation is $\sim 98\%$ of that of the unperturbed jet (dc control signal) under the same pressure. The initial perturbation amplitude of the jet (see later) is much smaller than the jet radius and is well within the linear regime.

The jetting fluid was ultrapure water (Milli-Q A-10, Millipore), analytical grade ethanol (>99.9% Fisher) and ethanol-water mixtures (5%, 10%, 20%, 50% ethanol by weight). The densities of the samples were obtained from Perry's Chemical Engineer Handbook where the values at 22 °C were extrapolated from the value of 20 °C and 25 °C. The viscosity was measured with a Cannon-Ubbelohde viscometer with a viscosity range of 0.8–4 mPa s. The equilibrium surface tension of the samples was measured by drop-shape analysis (FTA 200, First Ten Ångströms).

Confocal and conventional imaging systems share the same objective and tube lenses, with a flip mirror to switch between the two modes. A superluminescent diode (SLD, Newport SLD830-15-50-P) with peak emission at $\lambda_L = 860$ nm and power of 15 mW is used as a light source for confocal imaging. The output from a single-mode fiber with an angled physical contact is coupled to a fiber collimator and expanded to a diameter of 7.1 mm. The light is focused onto the jet through an infinity corrected, long working distance (WD), objective lens (WD = 17 mm, NA = 0.3, clear aperture = 6.3 mm). The backscattered light from the sample is

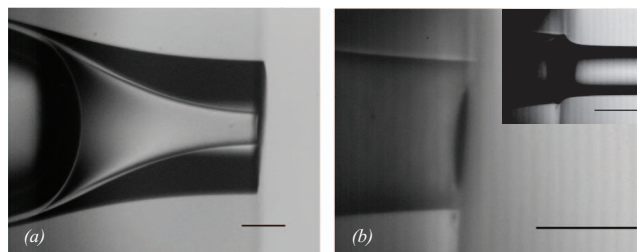


FIG. 2. Images of nozzle with an internal diameter of 100 μm obtained by conventional imaging with an objective lens with a NA of (a) 0.1, (b) 0.3. (Inset in (b)) Unperturbed liquid jet with the mean velocity of 5.7 m s⁻¹. Scale bars (a) 200 μm and (b) 100 μm .

collected by the same objective and then focused onto a 40- μm diameter pinhole through a tube lens with a focal length of 20 cm. The pinhole size matches the Airy disc of the focusing beam (radius = 34 μm) to achieve the best signal-to-noise ratio. The pinhole is positioned conjugate to the focus of the objective lens so that the signals that arise from the focus pass through the pinhole and the signals from the out-of-focus regions are largely blocked. The signal is detected by a photomultiplier tube (Hamamatsu H5783-20), electronically amplified with a home-built, wide bandwidth (dc–50 MHz) amplifier (gain of 60 dB) and sent to a gate generator (Stanford Research SR250). The gate generator is triggered by the signal generator. The output from the gate generator shows the exact timing relation of the sample gate with respect to the detected jet signal which are both sent to an oscilloscope (LeCroy 9304A, 200 MHz) for data processing.

For conventional imaging, an illuminator (Leica CLS 100) is used as light source with a spot size of 5-mm diameter on the jet. A fast shutter speed CCD camera (Jai M10SX) with a minimum exposure time of 1 μs records the bright-field image of the jet with single shot. Fine adjustment of the frequency of the signal generator close to the multiple of CCD frame rate yields a pseudo-sequence of images showing the evolution of drop formation.

III. METHODS AND EXPERIMENTAL RESULTS

A. Visualisation techniques

For conventional imaging, the objective NA of 0.3 yields a lateral resolution of 1 μm . Images of the 100- μm diameter orifice and unperturbed water jet (mean velocity of 5.7 m s^{-1}) emerging from the nozzle are shown in Fig. 2(b). The imaging system is calibrated with a graticule. The diameter of the nozzle is 100 μm in agreement with the manufacturer's specification. The profile of the surface of the jet near the nozzle derived from Fig. 2(b) is shown in Fig. 3. The nozzle plate is defined as $z = 0$ with z increasing down the jet. The jet diameter at the nozzle is $\sim 155 \mu\text{m}$ (in the presence of wetting) and contracts to a constant diameter of 103 μm , slightly larger than the nozzle diameter.

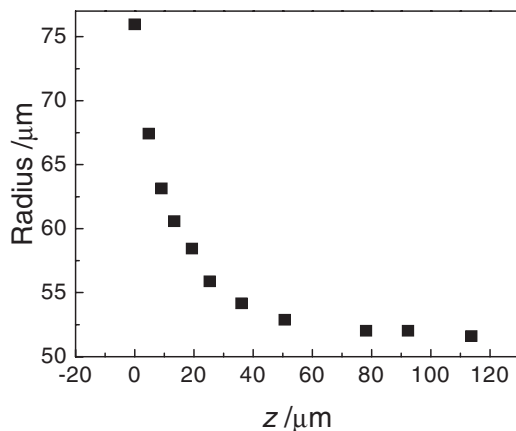


FIG. 3. Surface profile of unperturbed jet near the nozzle, obtained by conventional imaging. $u_0 = 5.7 \text{ m s}^{-1}$.

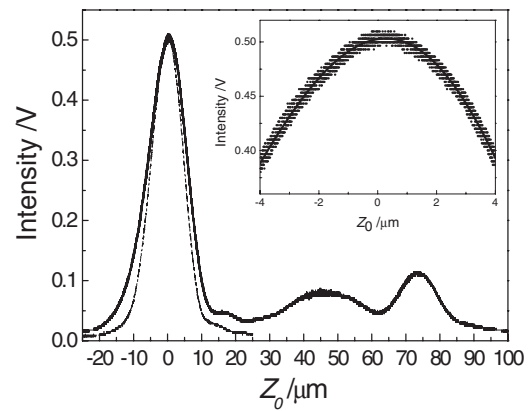


FIG. 4. Confocal response of a mirror (dashed) and an unperturbed water jet (solid) measured at the distance from nozzle $z = 1.0 \text{ mm}$. Z_0 is the coordinate along the optical axis of the confocal imaging system. The inset is a zoom-in of the axial response of the jet (points) with an asymmetric double sigmoidal fit (solid line).

The solid line in Fig. 4 shows the confocal response as the jet is scanned in a horizontal plane along the optical axis, Z_0 , of the laser beam, at a vertical jet position of $z = 1 \text{ mm}$. The three peaks from left to right correspond to the front surface, centre, and rear surface of the jet. The full width at half maximum (FWHM) of the detector response from the front surface of the jet when the jet is translated along the optical axis scan is 13.1 μm , which is slightly larger than the value of 11.2 μm measured from a planar mirror (dashed line in Fig. 4) due to the curved surface of the jet. The theoretical FWHM of the idealised confocal system with an infinitely small pinhole is $\sim \lambda_L / \text{NA}^2 = 9.5 \mu\text{m}$. With an asymmetric double sigmoidal fit to the axial response curve, the position of the surface can be determined at the peak with a resolution of 0.1 μm (see inset in Fig. 4). The accuracy to which the surface can be located is therefore limited to the repeatability of the translation stages (0.2 μm).

To achieve a higher resolution in surface profiling, the quasi-linear slope of the confocal response with respect to position along the optical axis can be used. Figure 5 shows that the time-averaged detector signal is well approximated by a linear function of Z_0 over a range of -7 to $-4 \mu\text{m}$ from the front surface reflection. Within this linear range, the displacement ΔD between two surfaces is proportional to the intensity difference of the detected signals ΔI , i.e., $\Delta D = \Delta I / S$, where S is the gradient of the plot in Fig. 5 with fitted value of $50.5 \pm 0.1 \text{ mV } \mu\text{m}^{-1}$. The resolution is limited by the mechanical stability of the nozzle, fluctuation of the light source, and electronic noise.

B. Determination of flow velocity uniformity

In Rayleigh's linear stability analysis, the jet is assumed initially to have a uniform velocity profile (plug flow). Bohr estimated the rate at which the difference in velocity between the centre and surface of the jet disappears.¹⁷ The initial velocity profile of a jet has a considerable effect on the jet breakup length: free falling jets with a fully developed parabolic initial velocity profile have greater kinetic energy

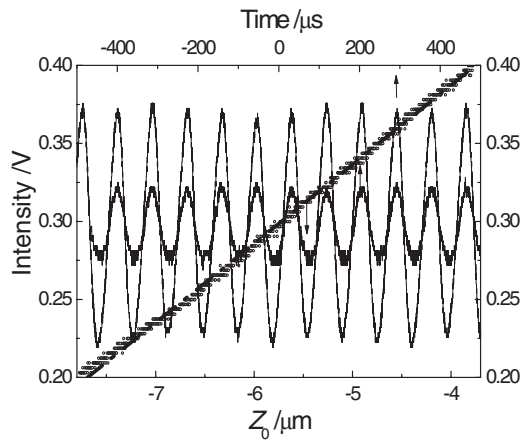


FIG. 5. Oscillation of a perturbed jet as a function of time (upper scale) at $z = 1$ mm (small amplitude wave) and $z = 2$ mm (large amplitude wave). Quasi-linear confocal response (points) of an unperturbed jet as a function of the position of the surface along the optical axis (lower scale) and a linear fit (dashed-dotted line), $f = 11.8$ kHz.

and are less stable and therefore shorter than jets with plug flow at the same mean flow rate.¹⁸ On the contrary, for oscillating jets the growth of the surface instability in a jet with a non-uniform velocity is damped and thus breakup is later than in jets with uniform velocity.^{19–21}

In order to validate the growth rate and dynamic surface tension measurements, we need to know whether the jet is in the plug flow regime. We have previously used laser Doppler velocimetry with two crossed laser beams to measure the velocity profile in mm-diameter jets²² but this method is not easily extendable to our present jet since the nozzle head obscures one of the beams. The approach we adopt here is to measure the temporal profiles of the scattered light from small particles seeded in the jet as the particles pass through a focused laser beam. A confocal pinhole is used to provide spatial resolution in the radial coordinate of the jet (i.e., the axial coordinate of the confocal microscope). The FWHM of the temporal profile Δt is inversely proportional to the velocity of the scattering particle and can be calibrated from measurements at large z where the velocity profile is fully relaxed.

Figure 6 shows the schematic of the optical setup. Collimated light from the SLD was gently focused onto the jet at an angle of 75° to the optical axis of the confocal microscope through an objective lens ($NA = 0.1$) with a beam waist at the focus of $5 \mu\text{m}$. A higher NA objective lens ($NA = 0.3$) collects the light scattered by the seed particles through the confocal imaging system. The seed particles were rutile (TiO_2) surface-treated with alumina-polyol (Kemira RODI) with a mean crystal size from transmission electron microscopy of 240 nm and a concentration of a few mg l^{-1} in water. The seed particles had no observable influence on the fluid surface tension and jet breakup. Figure 7 showed a typical temporal profile of the light scattered by a seed particle averaged over 200 events. The acquisition time was ~ 2 min.

The probe volume is defined by the overlap region of the two objective lenses. To optimize the overlap of the foci, we first pass the laser beam through the collection objective and use the confocal imaging property to locate the focus on the

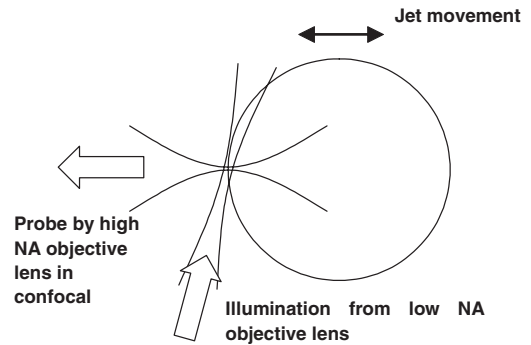


FIG. 6. Top view of geometry used to measure the jet velocity profile. A low NA objective lens, angled at 75° to the optical axis of the confocal microscope, is used for illumination. A high NA objective is used to detect the temporal profile of the light from a scattering particle.

surface. We then pass the laser beam through the illumination objective and adjust the position in order to maximize the frequency of scattering events and minimize the width of the temporal profile from a scattering particle.

Figure 8 plots Δt as a function of depth below the surface and distance from the nozzle for two jets with mean velocities of 5.7 m s^{-1} and 8.0 m s^{-1} . Note that at high z , where both jets are expected to show plug flow, Δt decreases with increasing depth below the surface. This trend arises from refraction of the illuminating beam by the surface of the jet: the nearer the illuminating laser is to the surface, the larger is the aberration due to refraction and the larger is the illuminated volume. The illumination geometry is independent of z , except in the immediate vicinity of the nozzle where the jet is still contracting ($z < 50 \mu\text{m}$). Therefore, the values of Δt at large z , where the velocity profile is known, can be used to generate calibration factors for the velocity profiles at all $z > 50 \mu\text{m}$. The depth resolution varies from $10 \mu\text{m}$ at the surface to $5 \mu\text{m}$ near the centre of the jet. Inspection of Fig. 8(a) shows that for the lower velocity jet, the velocity profile is independent of z for $z > 1$ mm, but that there is a small acceleration of the surface at lower z (larger Δt corresponds to a lower velocity). For the higher velocity jet [Fig. 8(b)], the velocity profile is independent of z , i.e., any deviations from plug flow are within

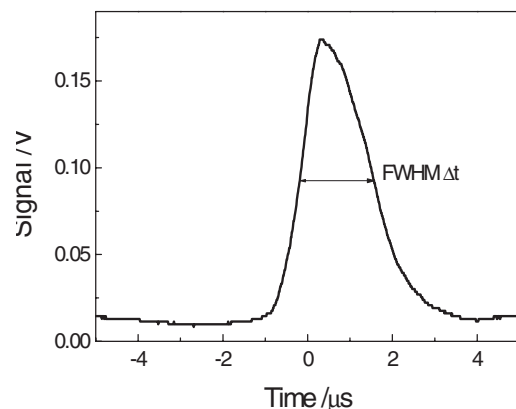


FIG. 7. Temporal profile of the scattered light from a seed particle averaged over 200 events. The FWHM of the pulse, Δt , is inversely proportional to the fluid velocity within the confocal volume.

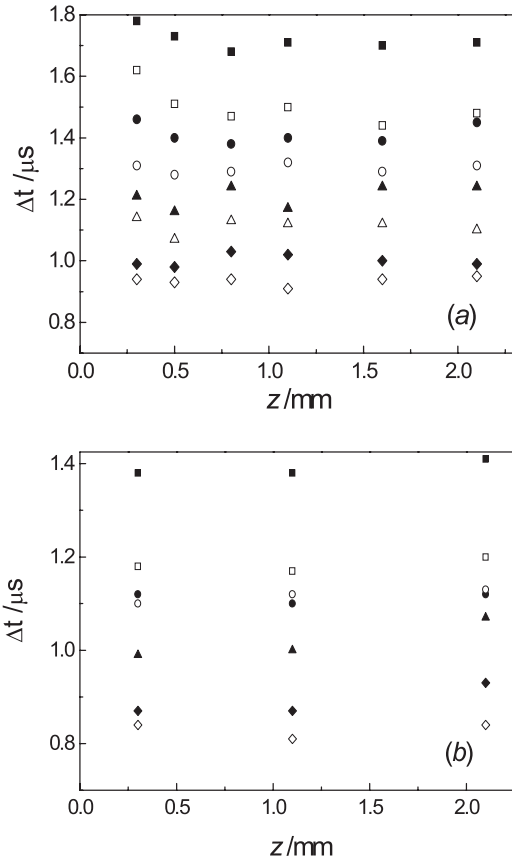


FIG. 8. Full width at half maximum, Δt , of the scattering from seed particles in an unperturbed jet as function of distance, z , from the nozzle for radial positions of $51.5 \mu\text{m}$ (■), $40.5 \mu\text{m}$ (□), $35.5 \mu\text{m}$ (●), $30.5 \mu\text{m}$ (○), $26.5 \mu\text{m}$ (▲), $21.5 \mu\text{m}$ (△), $17.5 \mu\text{m}$ (◆), and $8.5 \mu\text{m}$ (◇). (a) $u_0 = 5.7 \text{ m s}^{-1}$, $P = 30 \text{ kPa}$; (b) $u_0 = 8.0 \text{ m s}^{-1}$, $P = 60 \text{ kPa}$.

experimental precision. The data presented subsequently were acquired with a mean jet velocity u_0 of 5.7 m s^{-1} . We can therefore reliably assume plug flow for $z > 1 \text{ mm}$.

C. Growth rate measurement

Figure 9 shows conventional images of the water jet with a perturbation frequency, $f = 11.8 \text{ kHz}$ and wavelength of the induced perturbation, $\lambda = 480 \mu\text{m}$. A 0.1 NA objective lens was used to increase the field of view. The perturbation applied to the flow rate generates swells and necks. As the Laplace pressure varies inversely as the radius of curvature of the jet, the internal pressure increases at the neck and decreases at the swell, causing the fluid to flow from the neck to the swell. This flow exacerbates the instability and eventually causes the jet to break at the neck and form drops. According to Rayleigh's linear stability analysis, the radial displacement δ of a cylindrical jet of an incompressible inviscid liquid subject to infinitesimal axisymmetric oscillations of the surface grows exponentially if $2\pi a/\lambda < 1$, where a is the radius of the unperturbed jet and λ is the wavelength of the perturbation. It has the form of

$$\delta(z, t) = \delta \cos[k(z - u_0 t)] = \delta_0 e^{\alpha t} \cos[k(z - u_0 t)], \quad (1)$$

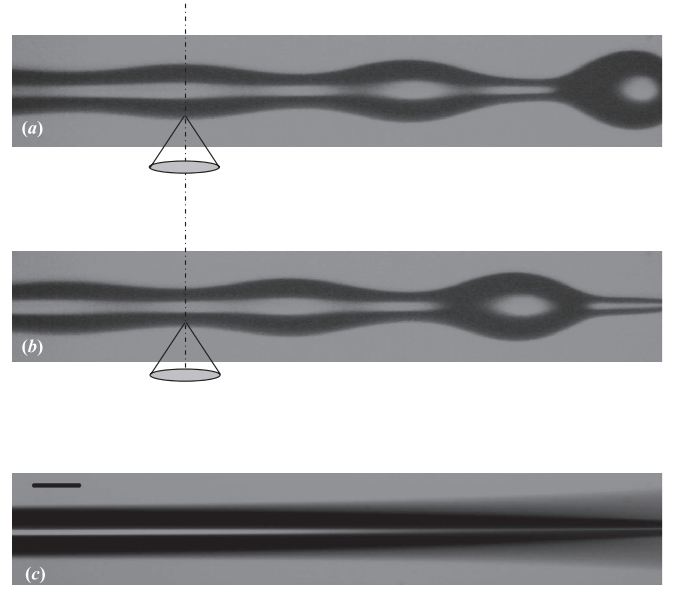


FIG. 9. Images that are conventionally used to determine the growth rate of the jet: (a) and (b) have an exposure time of $1 \mu\text{s}$ and are separated by an interval of $42 \mu\text{s}$. $f = 11.8 \text{ kHz}$. $\lambda = 480 \mu\text{m}$. (c) Overlay of many instantaneous images of an oscillating jet with an exposure time of 50 ms . Images have same magnification with a scale bar in (c) of $100 \mu\text{m}$. The sketched lens and beams in (a) and (b) focusing on the surface of the swell and the neck illustrate how the growth rate of the jet is determined by confocal microscopy.

where δ_0 is the initial amplitude of the disturbance, $u_0 = \lambda f$ is the jet velocity, α is the growth rate coefficient, and wavenumber $k = 2\pi/\lambda$. Weber deduced a dispersion relation between α and k for a Newtonian fluid²³

$$\alpha^2 \frac{ka}{2} \frac{I_0(ka)}{I_1(ka)} + \alpha v k^2 \left[2ka \frac{I_0(ka)}{I_1(ka)} \frac{l^2}{l^2 - k^2} - 1 - 2la \frac{I_0(la)}{I_1(la)} \frac{k^2}{l^2 - k^2} \right] = \frac{\sigma k^2 a^2}{2\rho a^3} (1 - k^2 a^2), \quad (2)$$

where $l^2 = k^2 + \alpha/v$; $v = \mu/\rho$; ρ , μ and σ denote the fluid density, viscosity, and surface tension; I_0 and I_1 are hyperbolic Bessel functions of the first kind of order 0 and 1. For $ka < 1$, $I_0(ka) \approx 1$, $I_1(ka) \approx ka/2$, and $l \gg k$. Equation (2) then reduces to a simplified quadratic equation

$$\alpha^2 + 3\alpha v k^2 - \frac{\sigma (ka)^2}{2\rho a^3} (1 - (ka)^2) = 0. \quad (3)$$

When the liquid viscosity vanishes, Eq. (2) reduces to Rayleigh's famous result for an inviscid liquid jet in a vacuum²

$$\alpha^2 = \frac{\sigma ka}{\rho a^3} (1 - k^2 a^2) \frac{I_1(ka)}{I_0(ka)}. \quad (4)$$

Taking the physical properties of water ($\rho = 998 \text{ kg m}^{-3}$, $\mu = 0.955 \times 10^{-3} \text{ Pa s}$ and $\sigma = 72.44 \text{ mN m}^{-1}$ at temperature of $22 \text{ }^\circ\text{C}$) and a jet diameter of $103 \mu\text{m}$, we obtain the growth rate α as a function of reduced wavenumber ka from Eq. (2), shown in Fig. 10 as a solid line with a maximum growth rate at $ka = 0.685$. The solution from Eq. (4) (assuming $\mu = 0$) is

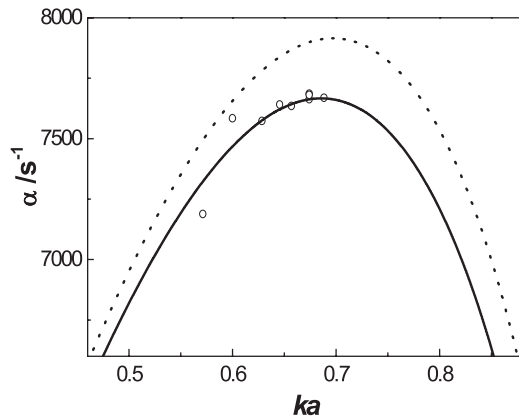


FIG. 10. Growth rate, α , of a water jet as a function of reduced wavenumber, ka calculated from Eq. (2) (solid line) for a viscous liquid and from Eq. (4) (dotted line) for an inviscid liquid. The open circles are determined from experiments in which the perturbation frequency was varied at a fixed $u_0 = 5.7 \text{ m s}^{-1}$.

also shown in Fig. 10 as a dotted line with a maximum growth rate at $ka = 0.697$ for comparison.

We are certainly not the first to measure the growth rate of the Rayleigh instability in liquid jets. Donnelly and Glaberson derived the growth rate by measuring the amplitude, δ , of successive oscillations, from half of the difference in radius difference between *neighboring* swell and neck, where the surface age, τ , is related to the distance from the nozzle by $\tau = z/u_0$.²⁴ They showed that the perturbation grows exponentially to within one wavelength of the disengagement of the drop from the jet. The growth rate was within 10% of the value predicted by Rayleigh's linear theory. Bellizia *et al.* pointed out that in order to remove second-order effects on the growth rate measurement, the radius of necks and swells should have been measured at the *same* axial location, z , on the jet,²⁵ which is not possible with frozen images of the type shown in Figs. 9(a) and 9(b). They demonstrated that such a measurement is achievable with a “non-strobed” image of perturbed jet captured by the camera over a period of time. We show the method in Fig. 9(c), where the image displays two contours of which the outer one envelops the swells and inner one envelops the necks. To calculate the growth rate, several points along the jet are picked and half of the difference in radius between the corresponding neck and swell, defined as the oscillating amplitude, is determined. The two contours in Fig. 9(c) show poor image contrast, however, which will induce an error of several micrometers in the amplitude of oscillation and hence cause uncertainty in the growth rate. From Fig. 9(c), we see that the separation of the two contours is only distinguishable from the seventh wavelength counted from the nozzle. As our jet exhibits plug flow after two wavelengths from the nozzle, we would lose information that could be used to determine the growth rate and surface tension more accurately.

With the confocal imaging system, we are able to measure δ from its very early stage with a precision of better than 4 nm, as we show below. This increased precision reduces the uncertainty in the growth rate measurement and makes the derived DST more reliable. It also makes it easier to detect

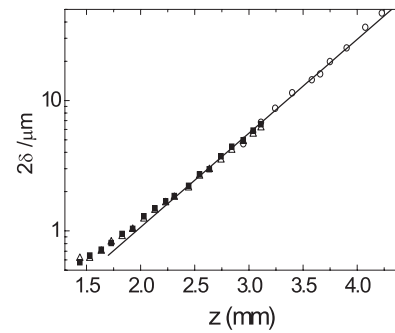


FIG. 11. Jet oscillation amplitude measured by three methods: CF1 (Δ), CF1+FFT (\blacksquare), and CF2 (\circ). $f = 10.3 \text{ kHz}$, $\lambda = 473 \text{ }\mu\text{m}$. The solid line is a linear fit to data for $2.5 \text{ mm} \leq z \leq 3.9 \text{ mm}$.

deviations from the theoretical predictions. The experimental approach is as follows. When the surface displacement of the corresponding neck and swell is $\leq 3 \text{ }\mu\text{m}$, which is normally the case for the first four wavelengths in our jet, we displace the front surface of the jet from the focal plane of the objective lens such that both the neck and swell are within the quasi-linear intensity response range (the dynamic range) of the confocal system. We keep the centre line of the wave in the middle of the confocal linear regime. The oscillating wave is detected in the time domain as shown in Fig. 5. The crest and trough of the sinusoidal wave correspond to the swell and neck for the same jet axial position, respectively. The uniformity of the wave indicates the good reproducibility of the oscillating jet. The amplitude of oscillation δ , can be readily derived from $\Delta I/2S$, where ΔI is the intensity difference between crest and trough. Figure 11 shows values of 2δ measured from $z = 1.4$ to 3.1 mm by this method, indicated as CF1. Each measurement is taken from a signal averaged over 100 sweeps. We actually measured the displacement of the swell and neck beyond the confocal dynamic range of $3 \text{ }\mu\text{m}$ (up to $7 \text{ }\mu\text{m}$) in order to check the validity of the method and compare it with other methods below. While we measure the intensity difference between crest and trough, we also record the fast Fourier Transform (FFT) amplitude of the fundamental signal averaged over 50 sweeps from the oscilloscope. For an ideal sinusoidal oscillation, the FFT amplitude is proportional to the oscillation amplitude. We calibrate the FFT signal against 2δ obtained by method CF1 within the confocal linear regime. These values of the oscillation amplitude are shown in Fig. 11 and labeled as CF1+FFT. The conversion factor from the amplitude of the FFT signal at the perturbation frequency and the oscillation amplitude, 2δ , is 89 nm/mV in our setup. As the background noise in the FFT is $20 \text{ }\mu\text{V}$, the CF1+FFT method could provide us the resolution of the displacement, 2δ , as small as 4 nm for a signal to noise ratio of 2. Near the nozzle, for $z \leq 1.5 \text{ mm}$, we noticed that harmonics are present in the FFT signal with the amplitude of the perturbation at the second harmonic comparable to the fundamental oscillation. However, the harmonics does not grow in the linear instability regime, the fundamental oscillation starts to dominate after $z \approx 1.6 \text{ mm}$ and gives very good agreement between the measurements in both frequency and time domains. When 2δ exceeds the dynamic range of $3 \text{ }\mu\text{m}$, the discrepancy between

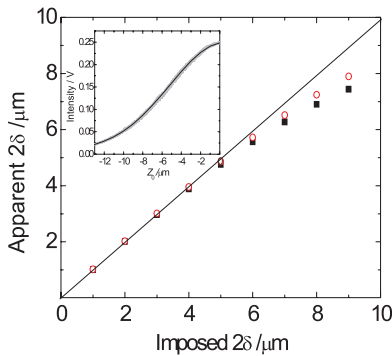


FIG. 12. Simulation of oscillation amplitude by CF1 (■) and CF1+FFT (○). The simulation is based on a sinusoidal wave with amplitude of δ falling into the confocal response regime with unperturbed surface at $Z_0 = -5.4 \mu\text{m}$. (Inset) Experimental confocal response curve (light grey line) and Gaussian fit (black line).

the two methods gets larger. We simulated the discrepancy between the two methods based on a sinusoidal wave with amplitude of δ falling within the confocal response regime for the unperturbed surface at $Z_0 = -5.4 \mu\text{m}$. We convert the displacement into a detected intensity using a Gaussian fit to the confocal response curve, shown in Fig. 12 inset. The intensity difference, ΔI , between the crest and trough of the wave can be derived from the imposed waveform and then compared with the value obtained by the two methods, CF1 and CF1+FFT. For CF1, the apparent value of 2δ is obtained from $\Delta I/S$ where the slope S has a fixed value of $25.38 \text{ mV}/\mu\text{m}$ obtained from a linear fit to the confocal response curve. For CF1+FFT, we simply take the FFT of the simulated light intensity and take the amplitude at the fundamental frequency. FFT amplitude agrees well with that of CF1 when $2\delta \leq 3 \mu\text{m}$. As expected both methods become less accurate as the oscillation amplitude increases beyond the confocal linear regime, shown in Fig. 12. However, for $2\delta = 4 \mu\text{m}$, the error is 40 nm for CF1+FFT and $0.1 \mu\text{m}$ for CF1. This analysis allows us to extend the dynamic range from $3 \mu\text{m}$ to $4 \mu\text{m}$ using CF1+FFT method with an error of 1% in the value of δ .

When 2δ exceeds $4 \mu\text{m}$, we have to adopt a new method for measuring the oscillation amplitude, which we do by locating the swell and neck *confocally*. The jet is translated along the optical axis of the confocal imaging system until the reflected signal from either the swell or the neck is maximized. Figure 13(a) shows the temporal response of the confocal signal when the microscope is focused on the swell. The peaks correspond to the appearance of the swell, the dips between the peaks to the necks. The delay on the gate output from boxcar was adjusted once so that $t = 0$ corresponds to the location of a swell. As we move upstream or downstream in multiples of the wavelength, the swell is always located at $t = 0$ within the linear regime, and this actually provides us with an accurate way of measuring the wavelength of the oscillation. As the amplitude of oscillation increases downstream of the nozzle, the peaks when the laser is focused on the swell become stronger and sharper as a result of the increasing curvature of the jet; conversely, the neck signal gets weaker due to the depth discrimination of a confocal microscope. Figure 13(b) shows the temporal profile when the confocal imaging system is focused on the neck, for the same

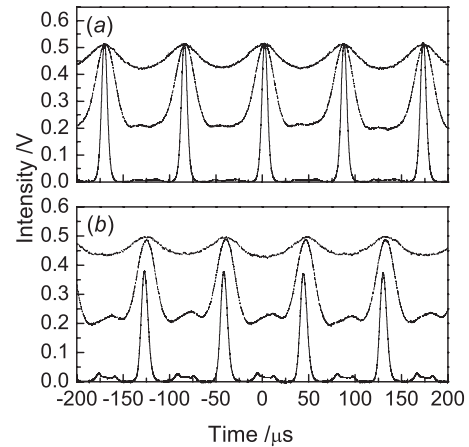


FIG. 13. Confocal signals when focusing on the swell (a) or the neck (b) at different axial position along the liquid jet: $z = 2.00 \text{ mm}$ (upper trace), 2.96 mm (middle trace), and 3.92 mm (lower trace). $u_0 = 5.7 \text{ m s}^{-1}$; $f = 11.8 \text{ kHz}$.

values of z . There is a phase difference of π between the swell and the neck, as one would expect in the linear instability regime.

When we scan the oscillating jet along the optical axis of the confocal imaging system, we obtain the confocal response curve shown in the inset to Fig. 14. The timebase of the oscilloscope and speed of the stage are adjusted to avoid aliasing of the wave. The top envelope of the signal from the confocal pinhole is extracted as shown in the main graph in Fig. 14 and a polynomial is fitted to the two maxima to obtain the locations of the swell and the neck, respectively. The displacement, 2δ , between the swell and neck can be determined with an accuracy of $0.2 \mu\text{m}$. We refer to this method as CF2. The values of 2δ obtained by CF2 are plotted against z in Fig. 11 and may be compared with CF1 and CF1+FFT. The main experimental error in CF2 arises from fluctuations in the jet. The measurements of 2δ by CF1, CF1+FFT and CF2 agree well at $2\delta \approx 4.6 \mu\text{m}$. For $2\delta \approx 5.6 \mu\text{m}$, CF1+FFT and CF2 still show good agreement while CF1 underestimates the amplitude of oscillation. As noted earlier, CF1+FFT is unreliable for $2\delta > 6 \mu\text{m}$.

Figure 11 plots values of 2δ as a function of z (on a semi-log plot) over two orders of magnitude in the

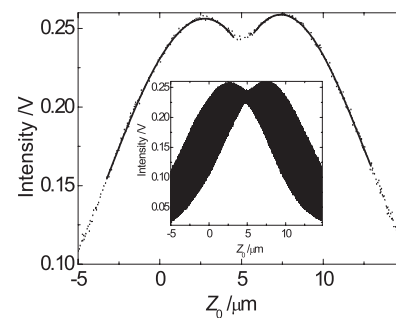


FIG. 14. Principle of the determination of the displacement of swell and neck by confocal scan method CF2. (Inset) Confocal response from the oscillating jet. Dotted line: top envelope of the response curves. The leftmost peak corresponds to the location of the swell and the rightmost peak to the neck. Solid line: polynomial fitting of the top envelope.

oscillation amplitude. From Eq. (1), the slope of this curve is equal to $\log_{10}(e) \times \alpha/u_0$, (where α is the growth rate and $u_0 = z/t$ the jet velocity) and is expected to be independent of z for a jet of constant velocity. While the data are accurately linear from $z = 2.5$ – 4.5 mm where $2\delta = 3$ – 50 μm , they clearly show a lower slope from $z = 1.5$ to 2.5 mm. The reason for this deviation from theory is unclear since the data in Fig. 8 show that the jet velocity is fully relaxed in this region.

In our experiments, we are measuring the growth of the instability in space but applying a model for the growth in time. Keller *et al.* have shown that the error of this approach is of the order of β^{-2} , where $\beta = u_0(\rho a/\sigma)^{0.5}$.²⁶ This analysis implies that a higher jet speed will give a better agreement between spatial and temporal instabilities. The highest speed for a 100 μm diameter jet running at wavenumber of 0.68 and perturbation frequency at its resonance of 11.8 kHz is 5.7 m s^{-1} which for a water jet gives $\beta = 4.8$, which is larger than the threshold of 3 suggested by Keller *et al.* We measured the growth rate of water jet for various values of ka , by variation of the jet perturbation frequency with fixed jet velocity of 5.7 m s^{-1} for $2\delta = 6$ – 60 μm . The growth rates are showed in Fig. 10. The measured values are in good agreement with Weber's theoretical predictions. We note that for those wavenumbers lying near the maximum in Weber's curve, the difference in the measured growth rate is almost indistinguishable. Nevertheless, different perturbation frequencies give different instability growth at the early stage ($2\delta < 4$ μm) leading to different jet break-off. The resonant frequency of 11.8 kHz gives the shortest break-off length. In the following surface tension measurement, we fixed the perturbation frequency to 11.8 kHz and jet speed to 5.7 m s^{-1} .

D. Surface tension determination

Equation (2) relates the surface tension to the growth rate and physical parameters of the liquid jet. Figure 15 shows growth rate measurements on ethanol/water mixtures for $2\delta = 6$ – 60 μm . Table I lists the density, low shear viscosity, growth rate, dynamic surface tension, σ_{dyn} , and equilibrium surface tension, σ_{eq} , of the different mixtures. Equation (2) was used to determine σ_{dyn} from the slopes of the graphs of the amplitude of oscillation against z in Fig. 15. The mean surface age (defined as $\tau = z/u_0$ where z is measured at the middle of the linear part of the experimental data) lies in the range of 0.6 – 0.9 ms. The measured jet diameter of 103 μm

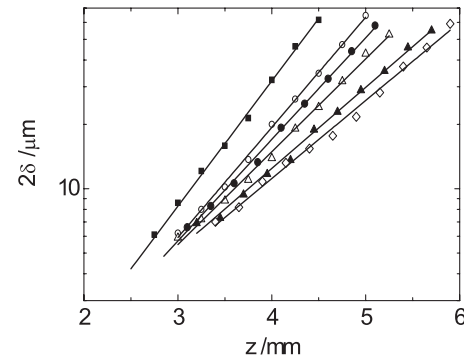


FIG. 15. Oscillation amplitude of ethanol/water binary mixtures: water (■), 5% (○), 10% (●), 20% (△), 50% (▲), and 100% ethanol (◇). $f = 11.8$ kHz. $\lambda = 480$ μm . $T = 22$ $^{\circ}\text{C}$.

and growth rate of 7665 ± 80 s^{-1} were used to obtain the surface tension of water of 72.6 ± 1.5 mN m^{-1} , in excellent agreement with the static value. The dynamic surface tension of pure ethanol and of 5% and 10% ethanol/water mixtures also agree to within experimental error with the equilibrium values. The main uncertainty in the determination of the DST comes from the uncertainty in the growth rate measurement, which is 1%–2%. The quadratic term is the largest term in Eq. (2), so the error in the surface tension is twice as large. The largest errors arise in liquids with the smallest surface tensions, with the result that the uncertainty in σ_{dyn} is roughly constant at 1.2 – 1.4 mN m^{-1} . It is worth noting the sensitivity of the DST to the jet diameter: a 1% error in the jet diameter leads to a 3% error in the DST. The unperturbed jet diameter was indistinguishable for all the water/ethanol solutions, but with an imaging resolution of ± 0.5 μm a systematic error of up to 2% is possible.

For the 20% and 50% ethanol/water mixtures, the deviation of the DST from the equilibrium value is significantly larger than the errors in the measurements: 4.7 mN m^{-1} and 6.5 mN m^{-1} , respectively. The growth rate measurements are reproducible: for example, two independent measurements of 50% ethanol/water mixtures yielded values of $\sigma_{\text{dyn}} = 34.6 \pm 1.5$ and 33.5 ± 1.5 mN m^{-1} . There are, *a priori*, three plausible explanations for the discrepancy between σ_{dyn} and σ_{eq} : concentration gradients in the jet, evaporative cooling and non-Newtonian fluid dynamics.

First, we consider the possibility that differential evaporation of ethanol and water leads to a surface composition that

TABLE I. Properties of liquid jets and derived values of the dynamic surface tension for ethanol/water mixtures.

Ethanol/water concentration		ρ (10^3 kg m^{-3})	μ (mPa s)	α (s^{-1})	Surface age (ms)	σ_{dyn} (mN m^{-1})	σ_{eq} (± 0.5 mN m^{-1})	$\sigma_{\text{dyn}} - \sigma_{\text{eq}}$ (mN m^{-1})
wt. % ethanol	Mole fraction X_E^b							
0	0	0.998	0.96	7665 ± 80	0.6	72.6 ± 1.5	72.4	0.2 ± 1.5
5	0.020	0.989	1.28	6835 ± 80	0.7	58.7 ± 1.4	57.0	1.7 ± 1.4
10	0.042	0.981	1.62	6200 ± 85	0.8	49.6 ± 1.4	48.6	1.0 ± 1.4
20	0.089	0.968	2.20	5800 ± 80	0.8	45.2 ± 1.3	40.5	4.7 ± 1.3
50	0.281	0.910	2.39	5115 ± 90	0.9	34.6 ± 1.2	28.1	6.5 ± 1.2
100	1	0.787	1.14	4742 ± 90	0.9	23.7 ± 1.2	22.3	1.4 ± 1.2

differs from the bulk composition, and hence has a higher surface tension. Due to the complexity of the jet hydrodynamics and aerodynamics, we use an evaporation law for a free falling droplet to estimate the effect of evaporation on the behavior of oscillating liquid jets. Fuchs derived an expression for the diffusion-controlled evaporation rate of a freely falling droplet²⁷

$$-\frac{dD^2}{dt} = \frac{8D_{va}M_wP_v(1-\phi)}{RT\rho} \left(1 + 0.3\text{Re}^{\frac{1}{2}}\text{Sc}^{\frac{1}{3}}\right), \quad (5)$$

where D is the droplet diameter; D_{va} is the diffusion coefficient of the vapour in air, i.e., 2.6×10^{-5} and $1.3 \times 10^{-5} \text{ m}^2 \text{ s}^{-1}$ for water and ethanol, respectively; M_w is the molecular weight; P_v is the equilibrium vapour pressure of the liquid, i.e., 2.65 and 6.55 kPa for water and ethanol at 22 °C, respectively. ρ is the density of the liquid. R is the gas constant and T is the absolute temperature. The Reynolds number $\text{Re} = Du_0/\nu_a$ and the Schmidt number $\text{Sc} = \nu_a/D_{va}$, where ν_a is the kinematic viscosity of the air, $1.53 \times 10^{-5} \text{ m}^2 \text{ s}^{-1}$ at 22 °C. ϕ is the relative humidity in ambient atmosphere, i.e., 0.5 for water and 0 for ethanol. Consider a 100- μm diameter droplet in free fall for 1 ms at a velocity $u_0 = 5.7 \text{ m s}^{-1}$, from Eq. (5) we obtain a surface depletion rate, $\pi dD^2/dt$, of $1.6 \times 10^{-8} \text{ m}^2 \text{ s}^{-1}$ and $1.5 \times 10^{-7} \text{ m}^2 \text{ s}^{-1}$ for water and ethanol, respectively. The diameter of the droplet will decrease by 0.24 μm for pure ethanol and by one-tenth of this amount for pure water. In our following analysis, we will neglect the evaporation of the water and consider only the effects of the evaporation of the ethanol. For the droplet of a binary mixture, the vapour pressure has a large position deviation from Raoult's law²⁸ especially for $X_E = 0.28$ (i.e., 50 wt. % ethanol) where the partial vapour pressure of ethanol is $P_v = 3.7 \text{ kPa}$ at 22 °C. Evaporation flux $J = \rho/(4M_wD)dD^2/dt$ of ethanol is estimated to be $1.2 \text{ mol m}^{-2} \text{ s}^{-1}$. We assume this evaporation flux is for ethanol only and is balanced by the diffusion flux of ethanol molecules. The diffusion length, l , of ethanol in the ethanol/water mixture after lifetime of $t = 1 \text{ ms}$ is $\sqrt{D_{\text{EtOH}}t}$, where D_{EtOH} is the diffusion coefficient of ethanol in the mixture ($1.3 \times 10^{-9} \text{ m}^2 \text{ s}^{-1}$),²⁹ i.e., $l \sim 1.1 \mu\text{m}$. The difference, Δc , of ethanol concentration between the bulk and sub-surface can be estimated by balancing the diffusive fluxes in the liquid and vapour phases: $\Delta c = J/D_{\text{EtOH}} \approx 1 \times 10^3 \text{ mol m}^{-3}$. For $X_E = 0.28$, the bulk ethanol concentration is $1.0 \times 10^4 \text{ mol m}^{-3}$. So the sub-surface concentration of ethanol is considerably ($\sim 10\%$) lower than the bulk concentration and the surface tension is correspondingly higher. For the bulk ethanol concentration of $X_E = 0.28$, the estimated sub-surface concentration in mole fraction will be 0.23. This will give us an increased surface tension by about 1.5 mN m^{-1} . While this estimate is far from quantitative it does suggest that the deviation between the dynamic and equilibrium surface tensions may arise from limitations on the mass transport of ethanol to the surface of the jet.

The second possible explanation for the discrepancy between σ_{dyn} and σ_{eq} is evaporative cooling, since the surface tension increases with decreasing temperature. The cooling effects will be most severe for pure ethanol so we take a free

falling ethanol droplet of 100 μm in diameter as an example. The loss of the mass Δm after 1 ms is $3 \times 10^{-12} \text{ kg}$. The heat loss Q will be $L \times \Delta m$, where $L = 855 \text{ kJ kg}^{-1}$ is the latent heat of evaporation of ethanol. The thermal diffusion length, l_h , in 1 ms is $l_h = \sqrt{k_{\text{EtOH}}t} = 9.4 \mu\text{m}$ and $k_{\text{EtOH}} = 8.9 \times 10^{-8} \text{ m}^2 \text{ s}^{-1}$ is the thermal diffusivity of ethanol. Assuming that the heat loss arises solely from the ethanol within a distance l_h of the surface, the temperature difference, ΔT , between the bulk and the surface is $\Delta T = Q/(\pi D^2 l_h \rho c_p)$, where is the thermal diffusion length and c_p is the thermal capacity of ethanol $2.4 \times 10^3 \text{ J kg}^{-1} \text{ K}^{-1}$. The estimated surface temperature will be about 5 K lower than the bulk. This will contribute a surface tension increase of $\sim 0.5 \text{ mN m}^{-1}$.³⁰ However, the surface cooling will lower the vapor pressure and slow down the evaporation rate at the surface. The net effect of evaporative cooling on the surface tension measurement would therefore be smaller than 0.5 mN m^{-1} . Given that the pure ethanol is a worst case and, in any event, the measured value of the dynamic surface tension is in good agreement with the static value, it is unlikely that evaporative cooling is the reason for the discrepancy between the equilibrium and dynamic surface tensions of the mixtures.

The third explanation for the discrepancy between σ_{dyn} and σ_{eq} is that viscosity at the high shear rates ($\sim 10^5 \text{ s}^{-1}$) inside the nozzle is lower than the low shear viscosity measured by the Cannon-Ubbelohde viscometer. Ethanol/water mixtures exhibit a pronounced nonlinear dependence of the bulk viscosity on the ethanol concentration (Table I). It is believed that at ethanol concentration X_E of higher than 0.1 the two components do not mix ideally at the molecular level, leading to the formation of disconnected water and ethanol clusters.^{31–33} It is possible that this structure breaks down under the high shear conditions of the jet, leading to a lowering of the dynamic viscosity. The dependence of the growth rate on the viscosity is not very strong, however: according to Eq. (2) the dynamic viscosity would need to be reduced by around 50% from its low-shear value to generate agreement between σ_{dyn} and σ_{eq} . In addition, the actual growth rate measurements are made in a region where the jet experiences low shear. Nevertheless, viscosity measurements at high shear rates would be useful to establish whether shear thinning could contribute to the observed deviations from the equilibrium surface tensions.

E. Pinch-off and satellite drop formation

As the oscillating jet approaches its breakup point, the surface deformation becomes asymmetric.^{34,35} The neck elongates into a ligament, which breaks off either at the fore or the aft side of the drop. The remaining ligament may be adsorbed into the following (or preceding drop), or the second end of the ligament may rupture to generate a satellite drop. In our experiments, where the perturbation amplitude is small (1% of the jet radius), the neck moves towards the forward main drop and eventually pinches off first at the fore side and then the aft side of the ligament, leading to the formation of a satellite drop [Fig. 16(b)]. To understand the nonlinear processes leading to satellite formation and for the

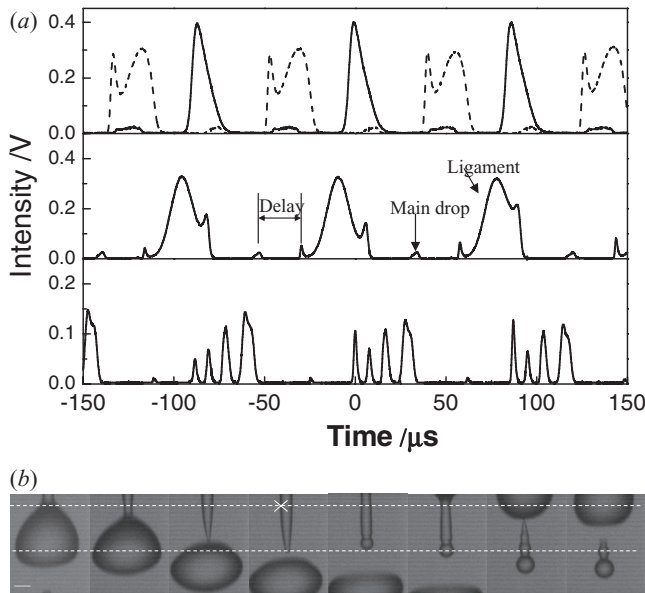


FIG. 16. (a) Temporal evolution of oscillating jet at different distances, z , from nozzle when focusing on the ligament. (Top) $z = 4.180$ mm (solid line) and 4.447 mm (dashed line), (middle) $z = 4.571$ mm, and (bottom) $z = 4.700$ mm. (b) Image sequence in the vicinity of jet breakup. Time interval between images = $10 \mu\text{s}$. $u_0 = 5.7 \text{ m s}^{-1}$. Scale bar = $50 \mu\text{m}$. The dotted lines correspond to $z = 4.571$ mm (upper) and $z = 4.700$ mm (lower). The cross in the fourth image indicates the location of the laser focus in the confocal imaging system at different z .

comparison of computer simulations with the performance of real jets, detailed observations of the jet breakup with high spatial and temporal resolution are required. Stroboscopic methods³⁶ and single flash imaging techniques⁵ provide images of the jet with a spatial resolution of $1 \mu\text{m}$ and an observation interval of $1 \mu\text{s}$. Our confocal imaging system allows us to follow the evolution of the neck in the time domain and to study the jet breakup with a higher temporal resolution.

Figure 16(a) shows the temporal profile of the reflected laser from the water jet when the laser beam is focused on the neck of the jet for a series of distances from the nozzle, z . At $z = 4.180$ mm (top trace, solid line), there is a single sharp peak corresponding to a single concave neck, but shape of the neck is already asymmetric [compare with the symmetric profiles for $z = 2.00, 2.96,$ and 3.92 mm shown in Fig. 13(b)]. By $z = 4.447$ mm (dashed line in top panel), the confocal response has developed two peaks: the broad peak corresponds to reflection from the quasi-cylindrical ligament while the sharp peak arises from the pinch point that is beginning to develop at fore end of the ligament. In the trace at $z = 4.571$ mm, which is close to the point at which the ligament detaches from the following drop, the neck shows three peaks. The two ‘horns’ on the main peak observed at $z = 4.571$ mm relate to the two pinching necks shown in the second and sixth images in Fig. 16(b), where the focus is $\sim 18 \mu\text{m}$ from the jet axis; the broad peak in between is the ligament. The trace at $z = 4.700$ mm, the point where the ligament detaches from the forward drop, has four separated peaks. (Note that at $z = 4.700$ mm we kept the focal position the same as at $z = 4.571$ mm, i.e., $\sim 18 \mu\text{m}$ from the jet axis.) The four peaks observed at $z = 4.700$ mm (with time intervals of 8, 8, and

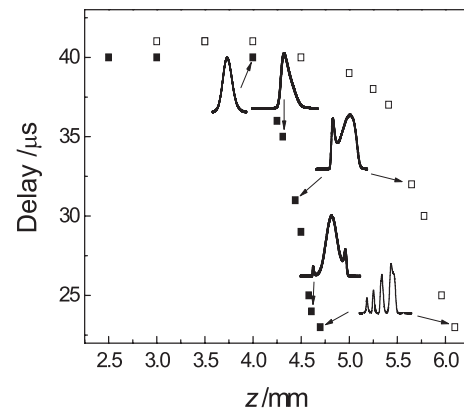


FIG. 17. Time delay between the swell and the following neck at the same axial position for the water (■) and ethanol (□) jets. The corresponding temporal profiles of the ligament from Fig. 16 are inserted.

$11 \mu\text{s}$) reflect the generation of subsidiary bulges and necks within the ligament, though these necks do not lead to subsequent fragmentation of the satellite drop.

The development of the asymmetry in the jet is shown in Fig. 17, which plots the time delay between the swell and the following neck at the same axial position of a water jet. The corresponding temporal profiles are inserted. For the water jet (solid square), from $z = 2.5$ – 4.0 mm, the delay remains nearly constant at $41 \mu\text{s}$, just less than half the perturbation period, and the temporal profile shows a single symmetric pulse. Further down the jet, the time delay between swell and the following neck decreases as the neck moves towards the forward drop. At $z = 4.44$ mm, the first pinch peak appears. The intensity of the reflected light from the fore pinch peak decreases as we move down the jet and disappears near the breakup point at $z = 4.70$ mm while bulges and necks form within the ligament. The time scale t_0 for the final stage of breakup measured from the first appearance of a pinch peak at $z = 4.44$ mm to eventual jet breakup at $z = 4.70$ mm is about half a wavelength, or $46 \mu\text{s}$. This agrees very well with the time scale given by the balance of surface tension and inertia at low viscosities,³⁷ i.e., $t_0 = (\rho a^3 / \sigma)^{1/2} = 43 \mu\text{s}$.

The temporal profile of ethanol jet is similar to the pure water one, but with a longer breakup length and a larger value of $t_0 \approx 80 \mu\text{s}$ due to the lower surface tension of ethanol. Indeed, the qualitative breakup behaviour of all the water/ethanol mixtures is the same: first pinch point develops at the fore end of the ligament, followed by rupture at the aft end to generate a single satellite drop. This observation shows that the surface tension affects the timescales of jet breakup but not the qualitative nature of the breakup.

IV. SUMMARY

We have presented a new approach to the study of instabilities in liquid jets by confocal imaging. The amplitude of oscillation of the jet was measured by three separate confocal methods from the earliest stages to the point of jet breakup. The achievable spatial resolution in the perturbed jet is far superior to conventional methods. The amplitude of oscillation of water and ethanol/water jets grows exponentially in time

from $2\delta = 6\text{--}60\ \mu\text{m}$ and is in good agreement with Weber's linear instability analysis. Close to the nozzle ($2\delta < 6\ \mu\text{m}$) the instability grows more slowly than expected from Weber's theory, for reasons that remain unclear. The dynamic surface tension of the pure water and ethanol/water mixture was derived from the measured growth rate at a surface age of 0.6–0.9 ms. The dynamic surface tensions for the pure solvents and for the 5% and 10% ethanol/water mixtures agreed well with the equilibrium surface tensions. For the 20% and 50% ethanol/water mixtures, the dynamic surface tension determined from Weber's equations was, however, significantly higher than the equilibrium value. Three possible explanations for the discrepancy were discussed and the most probable explanation is that the sub-surface concentration differs from the bulk concentration due to preferential evaporation of the more volatile component from the surface. The confocal imaging system was also used to observe the development of nonlinearities in the jet leading to asymmetric ligaments and satellite drops. Confocal imaging is a useful complementary tool to conventional imaging in the study of nonlinear jet instability dynamics.

The spatial resolution of the confocal imaging technique can be further improved with a higher NA objective lens and shorter wavelength light source. The system we describe has the potential to study instabilities in jets with diameters of only a few micrometers. The temporal resolution is limited by the response time of the photomultiplier tube, by the photon count rate and by the oscilloscope bandwidth. With appropriate choice of components, temporal resolution of 1 ns is achievable. This resolution allows the study of jets with high velocity, equaling or exceeding that of a commercial continuous inkjet with typical velocity of $20\ \text{ms}^{-1}$.

ACKNOWLEDGMENTS

The authors thank Mr. Appleby for designing the electronic circuits, Dr. Colegate for his help at an early stage of the experiments and Dr. Berson for helpful discussions on spatial instability and heat and mass transfer. This work was supported by Engineering and Physical Sciences Research Council (United Kingdom or UK) (EPSRC(GB)) Grant No. GR/T11920. We acknowledge useful discussions with many members of the Next Generation Inkjet Technology consortium.

¹J. Eggers and E. Villermaux, "Physics of liquid jets," *Rep. Prog. Phys.* **71**, 1–79 (2008).

²L. Rayleigh, "On the instability of jets," *Proc. London Math. Soc.* **10**, 4–13 (1878).

³L. Rayleigh, "On the capillary phenomena of jets," *Proc. R. Soc. London* **29**, 71–97 (1879).

⁴E. Becker, W. J. Hiller, and T. A. Kowalewski, "Experimental and theoretical investigation of large-amplitude oscillations of liquid droplets," *J. Fluid Mech.* **231**, 189–210 (1991).

⁵G. D. Martin, S. D. Hoath, and I. M. Hutchings, "Inkjet printing - the physics of manipulating liquid jets and drops," *J. Phys.* **105**, 1–14 (2008).

⁶A. H. Zewail, "Laser femtochemistry," *Science* **242**, 1645–1653 (1988).

⁷S. T. Thoroddsen, T. G. Etoh, and K. Takehara, "High-speed imaging of drops and bubbles," *Annu. Rev. Fluid Mech.* **40**, 257–285 (2008).

⁸T. G. Etoh, "A high-speed video camera of 4500 fps," *J. Inst. Image Inf. Telev. Eng.* **46**, 543–545 (1992).

⁹T. G. Etoh, D. Poggemann, G. Kreider, H. Mutoh, A. J. P. Theuwissen *et al.*, "An image sensor which captures 100 consecutive frames at 1000000 frames/s," *IEEE Trans. Electron Devices* **50**, 144–151 (2003).

¹⁰T. G. Etoh, D. V. T. Son, T. K. Akino, T. Akino, K. Nishi, M. Kureta, and M. Arai, "Ultra-high-speed image signal accumulation sensor," *Sensors* **10**, 4100–4113 (2010).

¹¹M. Minsky, U.S. patent #3013467 (December 19, 1961).

¹²T. Wilson and C. J. R. Sheppard, *Theory and Practice of Scanning Optical Microscopy* (Academic, London, 1984).

¹³M. Gu, *Principles of Three-Dimensional Imaging in Confocal Microscopy* (World scientific, London, 1996).

¹⁴D. K. Hamilton and H. J. Matthews, "The confocal interference microscope as a surface profilometer," *Optik* **71**, 31–34 (1985).

¹⁵C. Lee and J. Wang, "Noninterferometric differential confocal microscopy with 2 nm depth resolution," *Opt. Commun.* **135**, 233–237 (1997).

¹⁶L. Yang and C. D. Bain, "Liquid jet instability and dynamic surface tension effect on breakup," in *NIP25 and Digital Fabrication Technical Program and Proceedings* (Louisville, Kentucky, 2009), pp. 79–82.

¹⁷N. Bohr, "Determination of the surface-tension of water by the method of jet vibration," *Philos. Trans. R. Soc. London, Ser. A* **209**, 281–317 (1909).

¹⁸M. J. McCarthy and N. A. Molloy, "Review of stability of liquid jets and the influence of nozzle design," *Chem. Eng. J.* **7**, 1–20 (1974).

¹⁹S. J. Leib and M. L. Goldstein, "The generation of capillary instabilities on a liquid jet," *J. Fluid Mech.* **168**, 479–500 (1986).

²⁰W. Debler and D. Yu, "The break-up of laminar liquid jets," *Proc. R. Soc. London, Ser. A* **415**, 107–119 (1988).

²¹T. Jatzkowski and M. Modigell, "Experiments on axisymmetric oscillating water jets: absorption of ammonia in presence of n-pentanol surfaces," *Colloids Surf., A* **255**, 41–53 (2005).

²²T. Battal, C. D. Bain, M. Weiss, and R. C. Darton, "Surfactant adsorption and Marangoni flow in liquid jets. I. Experiments," *J. Colloid Interface Sci.* **263**, 250–260 (2003).

²³C. Weber, "Zum Zerfall eines Flüssigkeitssrahles," *Z. Angew. Math. Mech.* **11**, 136–154 (1931).

²⁴R. J. Donnelly and W. Gaberson, "Experiments on the capillary instability of a liquid jet," *Proc. R. Soc. London, Ser. A* **290**, 547–556 (1966).

²⁵G. Bellizia, C. M. Megaridis, M. McNallan, and D. B. Wallace, "A capillary-jet instability method for measuring dynamic surface tension of liquid metals," *Proc. R. Soc. London, Ser. A* **459**, 2195–2214 (2003).

²⁶J. B. Keller, S. I. Rubinow, and Y. O. Tu, "Spatial instability of a jet," *Phys. Fluids* **16**, 2052–2055 (1973).

²⁷N. A. Fuchs, *Evaporation and Droplet Growth in Gaseous Media* (Pergamon, London, 1959) pp. 41–42.

²⁸S. G. d'Ávila and R. S. F. Silva, "Isothermal vapor-liquid equilibrium data by total pressure method," *J. Chem. Eng. Data* **15**, 421–424 (1970).

²⁹L. Zhang, Q. Wang, and Y.-C. Liu, "On the mutual diffusion properties of ethanol-water mixture," *J. Chem. Phys.* **125**, 104502 (2006).

³⁰G. Vázquez, E. Alvarez, and J. M. Navaza, "Surface tension of alcohol + water from 20 to 50 °C," *J. Chem. Eng. Data* **40**, 611–614 (1995).

³¹Y. Amo and Y. Tominaga, "Low-frequency Raman study of ethanol-water mixture," *Chem. Phys. Lett.* **320**, 703–706 (2000).

³²S. Dixit, J. Crain, W. C. K. Poon, J. L. Finnery, and A. K. Soper, "Molecular segregation observed in a concentrated alcohol-water solution," *Nature (London)* **416**, 829–832 (2002).

³³J. H. Guo, Y. Luo, A. Augustsson, S. Kashtanov, J.-E. Rubensson, D. K. Shuh, H. Ågren, and J. Nordgren, "Molecular structure of alcohol-water mixtures," *Phys. Rev. Lett.* **91**, 157401 (2003).

³⁴W. T. Pimbley and H. C. Hee, "Satellite droplet formation in a liquid jet," *IBM J. Res. Dev.* **21**, 21–30 (1977).

³⁵J. Eggers, "Nonlinear dynamics and breakup of free-surface flows," *Rev. Mod. Phys.* **69**, 865–929 (1997).

³⁶T. A. Kowalewski, "On the separation of droplets from a liquid jet," *Fluid Dyn. Res.* **17**, 121–145 (1996).

³⁷M. C. Yuen, "Non-linear capillary instability of a liquid jet," *J. Fluid Mech.* **33**, 151–163 (1968).